

Expansion of the dynamic strain field in 3D-printed structures using a hybrid modeling approach

Miha Kodrič^a, Gregor Čepon^{a,*}, Miha Boltežar^a

^a*University of Ljubljana, Faculty of Mechanical Engineering, Aškerčeva 6, 1000 Ljubljana, Slovenia*

Abstract

The 3D printing of machine components is becoming an established technique. To ensure their robustness and longevity, it is crucial to numerically predict the dynamic response of these components in a variety of operating conditions. Dynamic properties are conventionally obtained in the form of displacement or strain-based response models. However, numerical modeling of the dynamic properties of 3D-printed structures can be a tedious task, mainly due to the complex geometry of the infill pattern and the influence of the printing parameters on the material and geometric properties. Alternatively, the dynamic properties can also be represented in the form of an experimental response model. This reflects the real dynamic properties, but is usually subject to measurement errors and has a low spatial resolution. To integrate the benefits of numerical and experimental response models, we propose a hybrid modeling approach with the System Equivalent Mixing method. The method was extended to a form that could integrate dynamic response models with different physical quantities (displacement and strain). The approach was then analyzed on a 3D-printed beam with a complex infill pattern, where an accurate expansion of the strain response to a high spatial resolution was demonstrated.

Keywords: Full-field strain response, Expansion process, PVDF strain sensor, 3D print, Modal analysis, Frequency response function,

1. Introduction

The designs of modern products and their methods of production must ensure that they are cheap to make and use. This can be achieved by employing innovative production approaches that allow rapid adaptation to customers' preferences and can adhere to guidelines relating to environmental acceptability and long-term use. Today, it is often possible to meet these requirements using 3D-printing technology.

3D printing was initially used for prototyping, but years of development have led to it becoming a procedure for regular production in some cases. 3D-printed structures have an excellent strength-to-weight ratio, great flexibility in terms of shape complexity, which means they can be used in a wide variety of applications [1]. New possibilities have opened up with the use of more advanced materials, enabling the construction of smart structures [2], actuators and sensors [3, 4].

*Corresponding author

Email address: gregor.cepon@fs.uni-lj.si (Gregor Čepon)

Simulating the dynamic response of 3D-printed structures is crucial to ensure their robustness and longevity in service. The dynamic properties are conventionally obtained with displacement-based response models. With the additional inclusion of a strain-response model, vital information with regards to the stresses can be obtained [5]. Therefore, by integrating both response models, more comprehensive information about the dynamic properties can be acquired.

Different approaches to numerical modeling have been developed to obtain the high-spatial-resolution dynamic response of 3D-printed structures. Predicting their dynamic behavior was investigated in detail in the numerical modeling of the dynamic crushing behavior of cellular structures [6, 7]. The finite element method with a detailed description of the complex infill geometry, was shown to be applicable for static response prediction [8] and even for predicting the natural frequencies of simple structures with a full infill [9]. To estimate the mechanical properties of 3D-printed structures using numerical modeling, methods based on computational intelligence are proposed in [10]. However, the common conclusion of all this research is that a numerical model of a 3D-printed structure is always associated with assumptions and simplifications. The main reason is the complex geometry (infill patterns) and a large number of influential printing parameters that affect the material and the dimensional properties of the final product [11]. Therefore, it is hard to develop valid numerical models that reflect the dynamic properties of a real, 3D-printed structure.

An alternative to the fully numerical approach is to access the dynamic properties of 3D-printed structures by using experimental modeling¹ [14, 15]. The advantage of this approach is that the structure is considered with fewer simplifications and assumptions; however, measurements are usually performed at only a limited number of points. Experimental modeling represents a trade off between experimental simplicity, accuracy and spatial resolution. For the full-field response, a non-contact vibration measurement method is used; the most popular being an optical method such as Digital Image Correlation [16, 17] or laser scanning [18, 19]. A promising non-contact alternative for measuring the dynamic response of structures is also the blade tip timing technique [20, 21]. It allows reconstruction of full-field dynamic strain of rotating blades from a limited set of measured strain responses. Measurement setups based on these approaches require relatively expensive equipment and an advanced post-processing procedure. They enable only a line-of-sight measurement, and thus the responses of any hidden components are inaccessible [22].

We propose an alternative, hybrid-based approach to modeling the dynamic properties of systems with a complex geometry (e.g., 3D-printed structures). The approach is based on the system equivalent model mixing (SEMM) method that integrates the experimental response model with a simplified numerical model [13]. The SEMM method is already applicable for joint identification [23], correction of noisy data from high-speed cameras and acoustic measurements [24, 25] and data-consistency identification [26, 27].

The numerical model involved to the SEMM method can be considerably simplified, since the accurate dynamic properties are inherited in the hybrid model by including the experimental response model. This approach has already been successfully applied to expand the translational experimental response model in [28]. However, in this article we investigated the possibility of expanding the experimental response model of the combined displacement and strain response using the SEMM method. This would allow the development of a simplified, homogenized numerical model of the 3D-printed structure without the need to model the geometry of the infill in detail. Low-cost, commercially available Piezoelectric Polyvinylidene Fluoride (PVDF) sensors were

¹The term experimental modeling refers to the process of obtaining an admittance matrix by direct measurement of FRFs on the structure [12, 13].

used to measure the strain frequency response functions as they are a good alternative to conventional piezoelectric strain sensors with built-in electronics (Integrated Electronics Piezo-Electric - IEPE) [29, 30]. The introduction of strain responses in the SEMM formulation is expected to be beneficial, as they are directly correlated with stresses and thus will enable better observability of the dynamic properties of the system [31, 32].

The paper is organized as follows. The following section briefly summarizes the theory of displacement and strain frequency response functions, followed by a short recap of the SEMM method. Next, in Section 4 is presented the full-field expansion using the SEMM method for mixing equivalent models of different physical quantities. Section 5 has an analysis of the proposed method on a 3D-printed beam. Finally, the conclusions are drawn in Section 6.

2. Displacement and strain frequency response functions

In general, a frequency response function (FRF) describes the relationship between the output response and the input excitation. Usually, the response is determined using displacement (u) sensors (accelerometers, laser vibrometers). In classical modal analysis, excitation is usually performed by applying a force (F) with a modal hammer or shaker. For a linear, undamped system with N_u response points and N_F excitation points with N_r identified natural frequencies ω_r , a steady-state response at observed frequency ω can be written as follows:

$$\mathbf{Y}^u(\omega) = \sum_{r=1}^{N_r} \frac{\mathbf{\Phi}_r^u \mathbf{\Phi}_r^{F\text{T}}}{\omega_r^2 - \omega^2} = \sum_{r=1}^{N_r} \frac{{}_r\mathbf{A}^u}{\omega_r^2 - \omega^2}, \quad (1)$$

where $\mathbf{\Phi}^u$ and $\mathbf{\Phi}^F$ are mass-normalized mode shapes at the locations of the displacement response and the force excitation, respectively. The ${}_r\mathbf{A}^u$ is the displacement modal constants matrix at the r -th natural frequency and can be written as follows:

$${}_r\mathbf{A}^u = \begin{bmatrix} \phi_{1,r}^u \phi_{1,r}^F & \cdots & \phi_{1,r}^u \phi_{j,r}^F & \cdots & \phi_{1,r}^u \phi_{N_F,r}^F \\ \vdots & \ddots & \vdots & \ddots & \vdots \\ \phi_{i,r}^u \phi_{1,r}^F & \cdots & \phi_{i,r}^u \phi_{j,r}^F & \cdots & \phi_{i,r}^u \phi_{N_F,r}^F \\ \vdots & \ddots & \vdots & \ddots & \vdots \\ \phi_{N_u,r}^u \phi_{1,r}^F & \cdots & \phi_{N_u,r}^u \phi_{j,r}^F & \cdots & \phi_{N_u,r}^u \phi_{N_F,r}^F \end{bmatrix}. \quad (2)$$

If all the excitation and displacement response points coincide, then $\mathbf{\Phi}^u = \mathbf{\Phi}^F$ since the displacement response and force excitation are complementary quantities and form interrelated modal constants [33]. Therefore, the modal constants matrix is symmetric (${}_r\mathbf{A}_{ij}^u = {}_r\mathbf{A}_{ji}^u$) and the FRF matrix \mathbf{Y}^u is symmetric ($\mathbf{Y}_{ij}^u = \mathbf{Y}_{ji}^u$). This means it is possible to obtain the displacement mode shape either at locations of the measured response (from the rows of the admittance matrix) or even at the locations of the performed excitations (from the columns of the admittance matrix).

Strain modal analysis relies on a measurement of the strain responses (ε). Hence, the FRF matrix presents the relationship between the strain response and the excitation force:

$$\mathbf{Y}^\varepsilon(\omega) = \sum_{r=1}^{N_r} \frac{\mathbf{\Phi}_r^\varepsilon \mathbf{\Phi}_r^{F\text{T}}}{\omega_r^2 - \omega^2} = \sum_{r=1}^{N_r} \frac{{}_r\mathbf{A}^\varepsilon}{\omega_r^2 - \omega^2}, \quad (3)$$

where Φ^ε and Φ^F are mass-normalized mode shapes at the locations of the strain response and the force excitation, respectively. The ${}_r\mathbf{A}^\varepsilon$ is the strain modal constants matrix at the r -th natural frequency and can be written as follows:

$${}_r\mathbf{A}^\varepsilon = \begin{bmatrix} \phi_{1,r}^\varepsilon \phi_{1,r}^F & \cdots & \phi_{1,r}^\varepsilon \phi_{j,r}^F & \cdots & \phi_{1,r}^\varepsilon \phi_{N_F,r}^F \\ \vdots & \ddots & \vdots & \ddots & \vdots \\ \phi_{i,r}^\varepsilon \phi_{1,r}^F & \cdots & \phi_{i,r}^\varepsilon \phi_{j,r}^F & \cdots & \phi_{i,r}^\varepsilon \phi_{N_F,r}^F \\ \vdots & \ddots & \vdots & \ddots & \vdots \\ \phi_{N_\varepsilon,r}^\varepsilon \phi_{1,r}^F & \cdots & \phi_{N_\varepsilon,r}^\varepsilon \phi_{j,r}^F & \cdots & \phi_{N_\varepsilon,r}^\varepsilon \phi_{N_F,r}^F \end{bmatrix} \quad (4)$$

The number of excitation points is still N_F and the number of strain response points is N_ε . Even if those points coincide the modal shapes obtained during excitation and at the strain-response points are no longer the same: $\Phi^\varepsilon \neq \Phi^F$. Therefore, the matrix of strain modal constants is no longer symmetric (${}_r\mathbf{A}_{ij}^\varepsilon \neq {}_r\mathbf{A}_{ji}^\varepsilon$) and neither is the strain FRF matrix ($\mathbf{Y}_{ij}^\varepsilon \neq \mathbf{Y}_{ji}^\varepsilon$).

From Eq. (2) it is evident that it is possible to identify only the displacement mode shapes from the displacement FRF matrix. Since the displacement response and the force excitation are complementary physical quantities, they hold the same information about the displacement mode shape. In the case of the measured strain response on the force excitation, it is possible to identify both the strain mode shape (from the rows of the admittance matrix) as well as the displacement mode shape (from the columns of the admittance matrix)², as is clear from Eq. (4).

3. System equivalent model mixing (SEMM)

The SEMM method was introduced by Klaassen et al. [13] and is based on the dynamic substructuring approach using Lagrange multiplier frequency-based substructuring (LM FBS) [34]. While the LM FBS method tries to couple the response models of multiple different structures, the SEMM method assembles equivalent models on a single substructure. For the sake of completeness, a basic recap of the theory of the LM FBS method is presented [35]. To consider n subsystems, all the local matrices are incorporated into a block-diagonal form. The equation of motion of the discrete dynamic subsystem in the frequency domain is:³

$$\mathbf{u} = \mathbf{Y}(\mathbf{f} + \mathbf{g}), \text{ where: } \mathbf{Y} = \begin{bmatrix} \mathbf{Y}^1 & & \\ & \ddots & \\ & & \mathbf{Y}^n \end{bmatrix}, \mathbf{u} = \begin{bmatrix} \mathbf{u}^1 \\ \vdots \\ \mathbf{u}^n \end{bmatrix}, \mathbf{f} = \begin{bmatrix} \mathbf{f}^1 \\ \vdots \\ \mathbf{f}^n \end{bmatrix}, \mathbf{g} = \begin{bmatrix} \mathbf{g}^1 \\ \vdots \\ \mathbf{g}^n \end{bmatrix}. \quad (5)$$

The vector of Degrees of Freedom (DoFs) is \mathbf{u} and represents the responses to the external force vector \mathbf{f} and \mathbf{g} is the vector of connecting forces with the other substructures to ensure equilibrium conditions. The admittance matrix of all the considered subsystems in block-diagonal form is denoted by \mathbf{Y} . The compatibility and equilibrium conditions are introduced with the signed Boolean matrix \mathbf{B} (Eq. (6)), where the interface forces are represented by the vector of Lagrange multipliers $\boldsymbol{\lambda}$.

$$\mathbf{B}\mathbf{u} = \mathbf{0}, \quad \mathbf{g} = -\mathbf{B}^T\boldsymbol{\lambda} \quad (6)$$

²The displacement-response mode shape is, in this case, actually the force-excitation mode shape, but since displacement and force are complementary physical quantities, it is the same as the displacement mode shape.

³An explicit dependency on frequency is omitted to improve the readability of the notation, as will be the case for the remainder of the paper.

Using the equilibrium and compatibility conditions and eliminating the Lagrange-multiplier vector $\boldsymbol{\lambda}$, the coupled structure's response is obtained, presenting the basic equation for the SEMM theory:

$$\mathbf{u} = \tilde{\mathbf{Y}} \mathbf{f} = \left[\mathbf{Y} - \mathbf{Y} \mathbf{B}^T (\mathbf{B} \mathbf{Y} \mathbf{B}^T)^{-1} \mathbf{B} \mathbf{Y} \right] \mathbf{f}. \quad (7)$$

The SEMM method is based on the parent model (Fig. 1a), providing the DoF set. The overlay model (Fig. 1b) introduces the real dynamic properties. To form the final hybrid model (Fig. 1d), the dynamic properties of the parent model are eliminated with the removed model (Fig. 1c).

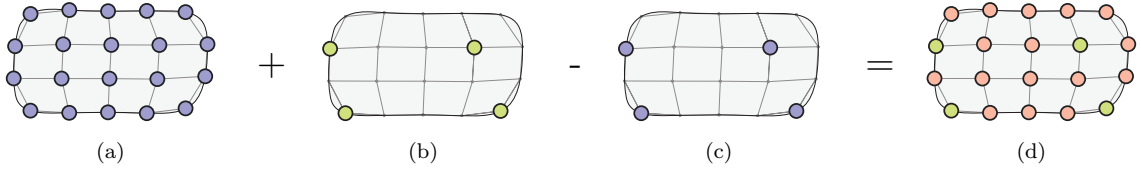


Figure 1: Equivalent models for SEMM method; a) Parent model \mathbf{Y}^{par} , b) Overlay model \mathbf{Y}^{ov} , c) Removed model \mathbf{Y}^{rem} , d) Hybrid model \mathbf{Y}^{SEMM} .

The procedure applies a substructuring approach to expand the model dynamics contained in an overlay model \mathbf{Y}_{ov} onto the DoF space of a parent model \mathbf{Y}_{par} [36]. Following Eq. (5) the response of the hybrid model can be formulated as:

$$\mathbf{u} = \mathbf{Y} (\mathbf{f} + \mathbf{g}), \text{ where: } \mathbf{Y} = \begin{bmatrix} \mathbf{Y}^{\text{par}} & \\ & -\mathbf{Y}^{\text{rem}} \\ & & \mathbf{Y}^{\text{ov}} \end{bmatrix}, \mathbf{u} = \begin{bmatrix} \mathbf{u}^{\text{par}} \\ \mathbf{u}^{\text{rem}} \\ \mathbf{u}^{\text{ov}} \end{bmatrix}, \mathbf{f} = \begin{bmatrix} \mathbf{f}^{\text{par}} \\ \mathbf{f}^{\text{rem}} \\ \mathbf{f}^{\text{ov}} \end{bmatrix}, \mathbf{g} = \begin{bmatrix} \mathbf{g}^{\text{par}} \\ \mathbf{g}^{\text{rem}} \\ \mathbf{g}^{\text{ov}} \end{bmatrix}. \quad (8)$$

The DoF set of the parent model contains the internal (i) and boundary (b) DoFs. The boundary DoFs must overlap with the overlay model so the dynamic coupling can be performed, while the internal DoFs of the parent model can be unique. The equivalent models appearing in the SEMM method are arranged by separating the internal and boundary DoFs in the admittance matrices:

$$\mathbf{Y}^{\text{par}} = \begin{bmatrix} \mathbf{Y}_{\text{ii}} & \mathbf{Y}_{\text{ib}} \\ \mathbf{Y}_{\text{bi}} & \mathbf{Y}_{\text{bb}} \end{bmatrix}^{\text{par}}, \quad \mathbf{Y}^{\text{ov}} = [\mathbf{Y}_{\text{bb}}]^{\text{ov}}, \quad \mathbf{Y}^{\text{rem}} = [\mathbf{Y}_{\text{bb}}]^{\text{par}}. \quad (9)$$

The process of dynamic decoupling of the removed model and the coupling of the overlay model to the parent model are achieved by applying compatibility and equilibrium conditions between all the models, just like for coupling the multiple subsystems (Eq. (6)).

$$\mathbf{B} = \begin{array}{c} \begin{array}{cccc} & \overbrace{\text{i}} & \overbrace{\text{b}} & \overbrace{\text{b}} & \overbrace{\text{b}} \\ & \text{---} & \text{---} & \text{---} & \text{---} \\ \mathbf{0} & \mathbf{I} & -\mathbf{I} & \mathbf{0} \\ \text{---} & \text{---} & \text{---} & \text{---} \\ \mathbf{0} & \mathbf{0} & \mathbf{I} & -\mathbf{I} \end{array} \\ \left. \begin{array}{l} \text{Decoupling} \\ \text{Coupling} \end{array} \right\} \\ \underbrace{\hspace{1.5cm}}_{\mathbf{Y}^{\text{par}}} \quad \underbrace{\hspace{1.5cm}}_{\mathbf{Y}^{\text{rem}}} \quad \underbrace{\hspace{1.5cm}}_{\mathbf{Y}^{\text{ov}}} \end{array} \quad (10)$$

Following the LM FBS methodology by eliminating the Lagrange multiplier and by considering the localization matrix, a reformulation to the primal notation is achieved. The single-line form of the basic SEMM method using primary admittance can be written as:

$$\mathbf{Y}^{\text{SEMM}} = [\mathbf{Y}]^{\text{par}} - \begin{bmatrix} \mathbf{Y}_{\text{ib}} \\ \mathbf{Y}_{\text{bb}} \end{bmatrix}^{\text{par}} (\mathbf{Y}^{\text{rem}})^{-1} (\mathbf{Y}^{\text{rem}} - \mathbf{Y}^{\text{ov}}) (\mathbf{Y}^{\text{rem}})^{-1} [\mathbf{Y}_{\text{bi}} \mathbf{Y}_{\text{bb}}]^{\text{par}}. \quad (11)$$

The basic SEMM method also has some extensions, increasing its robustness [13]. One of them is the ability to remove spurious peaks, which are a consequence of the conflicting dynamics between the models [36]. If the removed interface is extended to all the internal DoFs ($\mathbf{Y}^{\text{par}} = \mathbf{Y}^{\text{rem}}$), then the final form of the fully extended SEMM method in a single-line notation is:

$$\mathbf{Y}^{\text{SEMM}} = \mathbf{Y}^{\text{par}} - \mathbf{Y}^{\text{par}} ([\mathbf{Y}_{\text{bi}} \ \mathbf{Y}_{\text{bb}}]^{\text{rem}})^+ (\mathbf{Y}_{\text{bb}}^{\text{rem}} - \mathbf{Y}^{\text{ov}}) \left(\begin{bmatrix} \mathbf{Y}_{\text{ib}} \\ \mathbf{Y}_{\text{bb}} \end{bmatrix}^{\text{rem}} \right)^+ \mathbf{Y}^{\text{par}}. \quad (12)$$

4. Extension of the SEMM formulation for an expansion of the strain FRFs

In general the admittance matrix consists of combinations of excitations and responses. In structural dynamics, the excitation is usually performed using force or torque. The responses of the system are acquired by measuring the displacements (accelerate, mobility or receptance), rotations and strain. Every response type has its impact counterpart: displacement has force, rotation has torque and strain has stress. Theoretically, it is possible to generate the FRFs with torque and stress excitations, but it is nearly impossible to do this in practice [37, 38]. Therefore, the strain FRFs usually involve excitation with a force and measurement of the strain response. In this paper the extension of the SEMM method is proposed to be able to expand the strain responses. Here, an extended formulation is presented, where the displacement and strain FRFs are expanded simultaneously into a common hybrid model. The numerical model will hence contain the force impact and responses presented as a combination of displacements and strains:

$$\mathbf{Y}^{\text{num}} = \begin{matrix} & F \\ u & \left[\begin{array}{c} \mathbf{Y}^{u,F} \\ \hline \mathbf{Y}^{\varepsilon,F} \end{array} \right] \\ \varepsilon & \end{matrix}. \quad (13)$$

Following the original SEMM notation (Eq. (9)), the boundary and internal DoFs are divided to conduct the parent, removed and overlay model:

$$\mathbf{Y}^{\text{par}} = \begin{matrix} & \begin{matrix} \text{i} & \text{b} \\ \overbrace{F} & \overbrace{F} \end{matrix} \\ \begin{matrix} \text{i} \\ \text{b} \end{matrix} \left\{ \begin{matrix} u \\ \varepsilon \end{matrix} \right. & \left[\begin{array}{cc|cc} \mathbf{Y}_{\text{ii}}^{u,F} & \mathbf{Y}_{\text{ib}}^{u,F} & & \\ \mathbf{Y}_{\text{ii}}^{\varepsilon,F} & \mathbf{Y}_{\text{ib}}^{\varepsilon,F} & & \\ \hline \mathbf{Y}_{\text{bi}}^{u,F} & \mathbf{Y}_{\text{bb}}^{u,F} & & \\ \mathbf{Y}_{\text{bi}}^{\varepsilon,F} & \mathbf{Y}_{\text{bb}}^{\varepsilon,F} & & \end{array} \right] & , \mathbf{Y}^{\text{rem}} = \begin{bmatrix} \mathbf{Y}_{\text{bb}}^{u,F} \\ \mathbf{Y}_{\text{bb}}^{\varepsilon,F} \end{bmatrix} & , \mathbf{Y}^{\text{ov}} = \begin{bmatrix} \mathbf{Y}_{\text{bb}}^{u,F} \\ \mathbf{Y}_{\text{bb}}^{\varepsilon,F} \end{bmatrix} \end{matrix}. \quad (14)$$

Since the response and excitation DoFs are not fully aligned, it is necessary to impose the compatibility (c) and equilibrium (e) conditions separately using different signed Boolean matrices [23].

$$\mathbf{B}_c \mathbf{u} = \mathbf{0}, \quad \mathbf{g} = -\mathbf{B}_e^T \boldsymbol{\lambda} \quad (15)$$

The matrix \mathbf{B}_c defines the compatibility conditions, while the matrix \mathbf{B}_e determines the equilibrium conditions. The final equation for the LM FBS coupling/decoupling results in the following expression [12]:

$$\tilde{\mathbf{Y}} = \mathbf{Y} - \mathbf{Y} \mathbf{B}_e^T (\mathbf{B}_c \mathbf{Y} \mathbf{B}_e^T)^{-1} \mathbf{B}_c \mathbf{Y} \quad (16)$$

Regarding the presented division of the DoF on the internal and boundary together with further separation to displacement and strain DoF, the \mathbf{B} matrix must also be rewritten to ensure compatibility (c) and equilibrium (e) conditions between the equivalent models:

$$\mathbf{B}_c = \begin{array}{c} \begin{array}{cccc} \underbrace{\quad\quad}_i & \underbrace{\quad\quad}_b & \underbrace{\quad\quad}_b & \underbrace{\quad\quad}_b \\ \underbrace{u \quad \varepsilon}_{u} & \underbrace{u \quad \varepsilon}_{\varepsilon} & \underbrace{u \quad \varepsilon}_{u} & \underbrace{u \quad \varepsilon}_{\varepsilon} \end{array} \\ \left[\begin{array}{cccc|cc|cc} \mathbf{0} & \mathbf{0} & \mathbf{I} & \mathbf{0} & -\mathbf{I} & \mathbf{0} & \mathbf{0} & \mathbf{0} \\ \mathbf{0} & \mathbf{0} & \mathbf{0} & \mathbf{I} & \mathbf{0} & -\mathbf{I} & \mathbf{0} & \mathbf{0} \\ \hline \mathbf{0} & \mathbf{0} & \mathbf{0} & \mathbf{0} & \mathbf{I} & \mathbf{0} & -\mathbf{I} & \mathbf{0} \\ \mathbf{0} & \mathbf{0} & \mathbf{0} & \mathbf{0} & \mathbf{0} & \mathbf{I} & \mathbf{0} & -\mathbf{I} \end{array} \right] \begin{array}{l} \left. \vphantom{\left[\right.} \right\} \text{Decoupling} \\ \left. \vphantom{\left[\right.} \right\} \text{Coupling} \end{array} \\ \underbrace{\quad\quad\quad}_{\mathbf{Y}^{\text{par}}} \quad \underbrace{\quad\quad\quad}_{\mathbf{Y}^{\text{rem}}} \quad \underbrace{\quad\quad\quad}_{\mathbf{Y}^{\text{ov}}} \end{array} \quad (17)$$

$$\mathbf{B}_e = \begin{array}{c} \begin{array}{cccc} \underbrace{\quad\quad}_i & \underbrace{\quad\quad}_b & \underbrace{\quad\quad}_b & \underbrace{\quad\quad}_b \\ \underbrace{F}_{F} & \underbrace{F}_{F} & \underbrace{F}_{F} & \underbrace{F}_{F} \end{array} \\ \left[\begin{array}{ccc|c} \mathbf{0} & \mathbf{I} & -\mathbf{I} & \mathbf{0} \\ \hline \mathbf{0} & \mathbf{0} & \mathbf{I} & -\mathbf{I} \end{array} \right] \begin{array}{l} \left. \vphantom{\left[\right.} \right\} \text{Decoupling} \\ \left. \vphantom{\left[\right.} \right\} \text{Coupling} \end{array} \\ \underbrace{\quad\quad\quad}_{\mathbf{Y}^{\text{par}}} \quad \underbrace{\quad\quad\quad}_{\mathbf{Y}^{\text{rem}}} \quad \underbrace{\quad\quad\quad}_{\mathbf{Y}^{\text{ov}}} \end{array} \quad (18)$$

After performing linear-algebra operations between the defined matrices in Eq. (16) the final equation for the basic formulation of the SEMM method is obtained:

$$\mathbf{Y}^{\text{SEMM}} = \left[\mathbf{Y} \right]^{\text{par}} - \begin{bmatrix} \mathbf{Y}_{ib}^{u,F} \\ \mathbf{Y}_{ib}^{\varepsilon,F} \\ \mathbf{Y}_{bb}^{u,F} \\ \mathbf{Y}_{bb}^{\varepsilon,F} \end{bmatrix}^{\text{par}} (\mathbf{Y}^{\text{rem}})^+ (\mathbf{Y}^{\text{rem}} - \mathbf{Y}^{\text{ov}}) (\mathbf{Y}^{\text{rem}})^+ \begin{bmatrix} \mathbf{Y}_{bi}^{u,F} & \mathbf{Y}_{bb}^{u,F} \\ \mathbf{Y}_{bi}^{\varepsilon,F} & \mathbf{Y}_{bb}^{\varepsilon,F} \end{bmatrix}^{\text{par}}. \quad (19)$$

A similar procedure can also be performed for the fully-extended formulation, where the removed model is defined by the whole parent model, so it applies $\mathbf{Y}^{\text{par}} = \mathbf{Y}^{\text{rem}}$. The final equation of this

formulation has the following form:

$$\mathbf{Y}^{\text{SEMM}} = \mathbf{Y}^{\text{par}} - \mathbf{Y}^{\text{par}} \left(\begin{bmatrix} \mathbf{Y}_{\text{bi}}^{u,F} & \mathbf{Y}_{\text{bb}}^{u,F} \\ \mathbf{Y}_{\text{bi}}^{\varepsilon,F} & \mathbf{Y}_{\text{bb}}^{\varepsilon,F} \end{bmatrix}^{\text{rem}} \right)^+ \left(\begin{bmatrix} \mathbf{Y}_{\text{bb}}^{u,F} \\ \mathbf{Y}_{\text{bb}}^{\varepsilon,F} \end{bmatrix}^{\text{rem}} - \begin{bmatrix} \mathbf{Y}_{\text{bb}}^{u,F} \\ \mathbf{Y}_{\text{bb}}^{\varepsilon,F} \end{bmatrix}^{\text{ov}} \right) \left(\begin{bmatrix} \mathbf{Y}_{\text{ib}}^{u,F} \\ \mathbf{Y}_{\text{ib}}^{\varepsilon,F} \\ \mathbf{Y}_{\text{bb}}^{u,F} \\ \mathbf{Y}_{\text{bb}}^{\varepsilon,F} \end{bmatrix}^{\text{rem}} \right)^+ \mathbf{Y}^{\text{par}}. \quad (20)$$

5. Experimental case study

The presented methodology was tested on a laboratory beam-like structure, 3D printed with a Prusa i3 MK3S+ FFF (Fused-Filament Fabrication) printer. The printing involved a PLA filament with a diameter of 1.75 mm. The other printing settings are collected in Table 1. To prove the hypothesis that it is possible to extend the experimentally obtained displacement and strain FRF based on a SEMM expansion process, two beams were printed with different infill percentages, 20 % and 40 %, both with a Gyroid shaped infill (Fig. 2), which represents a complex pattern that is difficult to model numerically.

Table 1: Printing settings.

Parameter	Nozzle diameter	Layer height	Printing speed	Infill	Fill pattern	Nozzle temp.	Bed temp.
Value	0.6 mm	0.3 mm	Perimeter: 45 mm/s Infill: 70 mm/s	20 %, 40 %	Gyroid	210 °C	60 °C

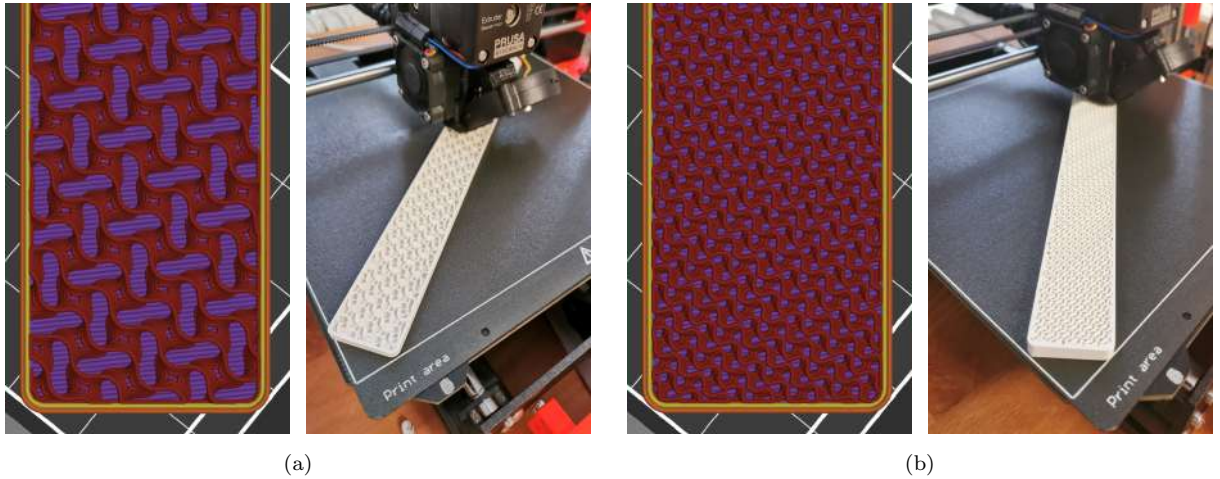


Figure 2: Infill pattern Gyroid in Prusa Slicer software and during the 3D-printing process; a) 20 % infill, b) 40 % infill.

5.1. Experimental response model

To obtain the FRF of the analyzed structures, we performed an experimental modal analysis measuring the displacement and strain response in terms of the force excitation. The structures were excited using a miniature modal hammer (PCB 086E80) with a sensor sensitivity of 23.53 mV/N. The applied forces were rather small, about between 10 and 15 N, so the response displacements were also small and still in the linear elastic range (the maximum displacement of the analyzed beams was $\approx 5 \mu\text{m}$). The displacement response was acquired using a laser vibrometer (Polytec PDV-100). It was set in the highest velocity range (500 mm/s with a sensitivity 125 (mm/s)/V) and was capable of detecting signals in the frequency range between 0.5 Hz and 22 kHz. It has 24-bit analogue-to-digital conversion in a voltage range of ± 4 V. The strain responses were measured using commercially available PVDF strain gauges.

The analyzed beam was divided into seven equidistant points, where the FRFs were measured (Fig. 3). The number of observed measurement points was determined by the size of the strain sensor. Here we proposed a relatively large number of sensors to obtain the dynamic response with high spatial resolution. The structure was excited at all seven points and the strain sensors were also placed at these locations. Strain gauges were placed on the bottom of the beam, while the excitations were performed on the top surface. The displacement response was measured at only one location at point 3 on the top surface of the beam (Fig. 4).

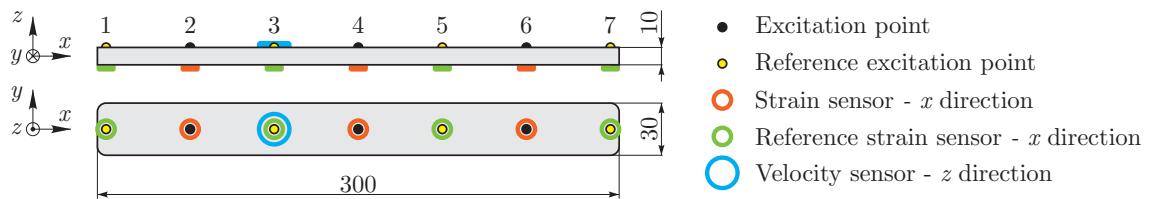


Figure 3: Schematic presentation of experimentally obtained locations.



Figure 4: Experimental setup.

The overlay model for the SEMM expansion included only the strain responses at points 2, 4 and 6 (in Fig. 3 marked with yellow dots and orange circles) and the displacement response at

point 3 (in Fig. 3 marked with a blue circle). The rest of the experimental locations served as a reference model, according to which the accuracy of the expansion was assessed.

5.1.1. PVDF strain gauges

The strain response of the 3D-printed structure was measured using PVDF strain sensors. Today, piezoelectric polymer sensors are widely used as switches, speakers, microphones [39]. They can also be used for vibrational testing [29]. Therefore, we acquired the strain FRFs using commercially available PVDF strain gauges. Their bimorph configuration is made of a $28 \mu\text{m}$ thick piezoelectric polymer film, connected to a 0.125 mm electrode (Fig. 5). PVDF sensors are small ($10 \times 15 \text{ mm}$), very flexible, enable a high voltage output, and can be used in a wide frequency range [39]. Another benefit of these highly flexible PVDF strain gauges is the ability to use them on slightly curved faces, which is not feasible with classic strain sensors that have quartz sensing elements in a titanium housing [40].

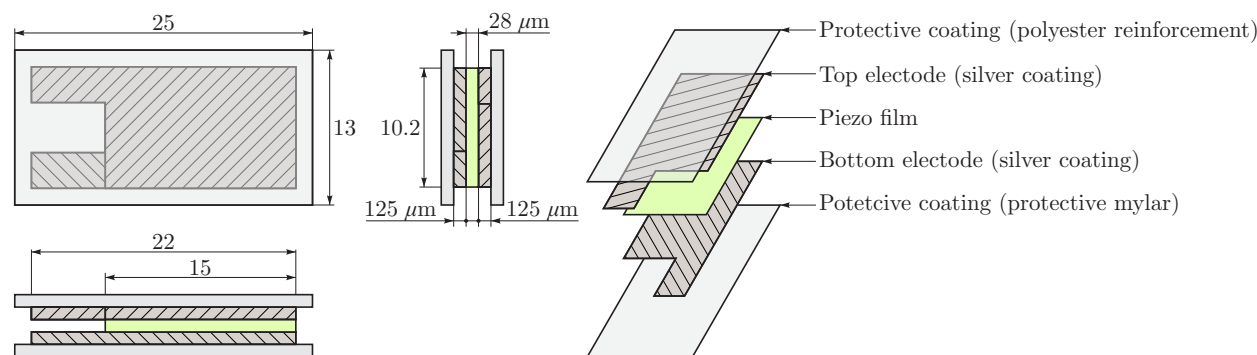


Figure 5: Schematic representation of strain gauge.

The measuring principle of strain gauges is based on averaging the strain through the contact surface. Therefore, the highest measured frequency is limited to the ratio of the corresponding strain mode shape's wavelength and the length of the strain sensor [40]. A PVDF sensor with a larger area has a larger output voltage and a better signal-to-noise ratio (SNR), but it is not suitable for detecting higher frequencies. On the other hand, the small sensor can detect high-frequency signals, but with weak output voltage, which results in a low SNR [29, 41].

The cross sensitivity of PVDF sensors was investigated in [41], where they showed that the longitudinal direction has a five-times-higher sensitivity compared to the transverse direction. However, the measured voltage will always be a result of the strain field due to Poisson's effect [40].

The PVDF strain sensors used have a nominal sensitivity of $205 \text{ mV}/\mu\epsilon$. They were calibrated on-site using a calibrated reference quartz strain sensor (PCB 740B02). The unknown sensitivity of the PVDF strain sensors was evaluated as the ratio between the PCB reference signal and the acquired PVDF voltage signal. The comparison of the two signals is shown in Fig. 6. Here, it can be seen that the response measured with the PVDF strain sensor is almost identical to the response of the PCB reference strain sensor. In addition, the signal from the PVDF sensor is less noisy in the anti-resonance regions where the PCB sensor has a slightly worse SNR. The reusable PCB strain sensor has a titanium housing and is therefore unable to accurately detect strain at higher frequencies with smaller magnitudes.

The PVDF strain sensors were attached to the structure using polycrylic glue. The generated voltage was measured using acquisition modules with a 16-bit resolution (NI 9215) mounted to the

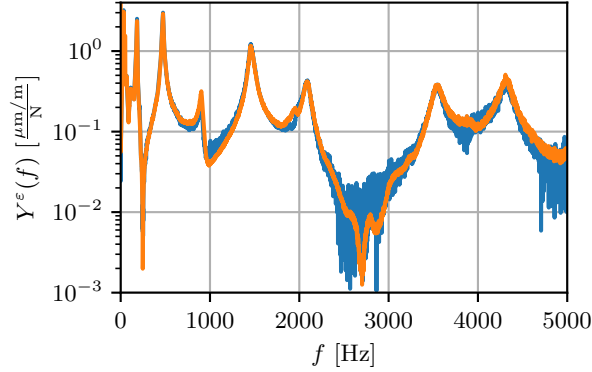


Figure 6: Comparison of strain response between reference PCB quartz strain sensor and PVDF strain sensor.
— - PCB strain sensor, — - PVDF strain sensor

measurement chassis (NI 9172). The signals were measured with a sampling rate of 50 kS/s. The sensors were connected to the acquisition system via a lead wire, and contact was made with a terminal block to allow simple assembly and disassembly (Fig. 7).

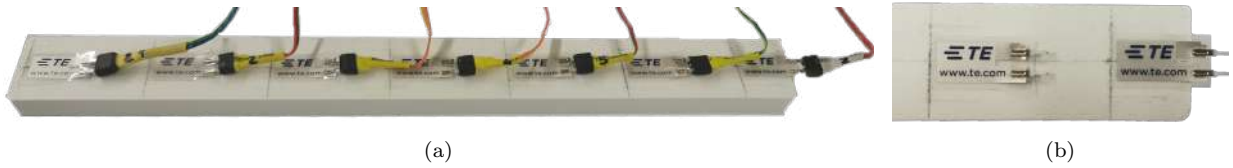


Figure 7: PVDF sensors attached to the testing beam; a) distribution of seven sensors, b) detailed presentation of the attached sensor.

5.2. Numerical response model

The numerical model was created by the finite element method (FEM) using the commercial software Ansys Workbench. We used linear material properties with linear 3D finite elements with 8 nodes. The sparse matrix solver used by the block Lanczos eigensolver is used to solve the eigenvalue problem on a single processor with four threads. The finite element model consisted of 5760 elements with a total of 7865 nodes. The numerical models were significantly simplified, compared to real 3D-printed beams, since we proposed a homogeneous material without a detailed description of the complex infill pattern's configuration. Attached measurement sensors were ignored in the numerical model to demonstrate that even a simple numerical model can serve as a sufficient basis for the expansion process with the proposed SEMM formulation. The outer dimensions were the same as in the experimental models. The model consists of 5760 linear finite elements with 8 nodes at each element (Fig. 8).

In addition, the material properties of the beam were considerably simplified, since the beam was modeled with isotropic material that has a uniform Young's modulus. For both experimental models, different numerical models were built, varying in material density, but with the same Young's modulus, approximated based on the findings in [11]. The density was calculated from the measured mass and known geometry. The main advantage of the proposed method is that even a highly simplified numerical model proposing isotropic material properties provides a sufficient

approximation to perform the accurate expansion process, since the real dynamic properties are integrated with the inclusion of the experimental response model. The properties of the material used are collected in Table 2. The system matrices were built using linear assumptions regarding material properties and proportional viscous damping. A value of 0.05 was assumed for the constant damping coefficient. This damping value is only a rough approximation, since the hybrid model inherits the damping properties of the experimental response model [28].

Table 2: Material properties of numerical models.

Parameter	Mass [g]	Density [kg/m ³]	Young modulus [MPa]
20 % infill	46	511	2500
40 % infill	66	733	2500



Figure 8: Finite-element model of the analyzed beam.

The FRF matrices of the numerical models were generated using the modal-superposition method, using the first 50 natural frequencies and the corresponding mode shapes to eliminate the effect of the modal truncation.

5.3. Results

The accuracy of the expansion process was evaluated with the reference experimental model that had a higher spatial resolution (7 measurement points). The frequency range of the analysis ranged between 100 and 3000 Hz. This frequency range was proposed as the first natural frequency is above 200 Hz and because of the poor SNR in the low frequency range due to the low strain values.

A comparison of the strain FRFs of the experimental and numerical models is presented in Fig. 9. Here, an evident FRF amplitude shift between the numerical and experimental results can be observed. The experimentally obtained strains are approximately $10\times$ lower than the numerical results due to the incorrect material and geometrical properties.

A comparison between the natural frequencies for the experimental and corresponding numerical models is presented in Table 3. The natural frequencies of the experimental model were identified using a multi-reference modal identification algorithm. The difference between the numerical and experimental natural frequencies is approximately 20 %. Even though there are some similarities in the FRF shape, the numerical model in the presented form is not directly suitable for further analysis since it does not reflect the dynamic properties of the real structure. Nevertheless, as was demonstrated in [28], it can be used for an expansion process with an experimental model.

5.3.1. Expansion process

Using the proposed SEMM expansion process, the experimentally obtained dynamic properties from a limited number of DoFs were extended to DoFs of the numerical model with a higher spatial resolution. We incorporated the proposed SEMM formulation into the Python open-source package

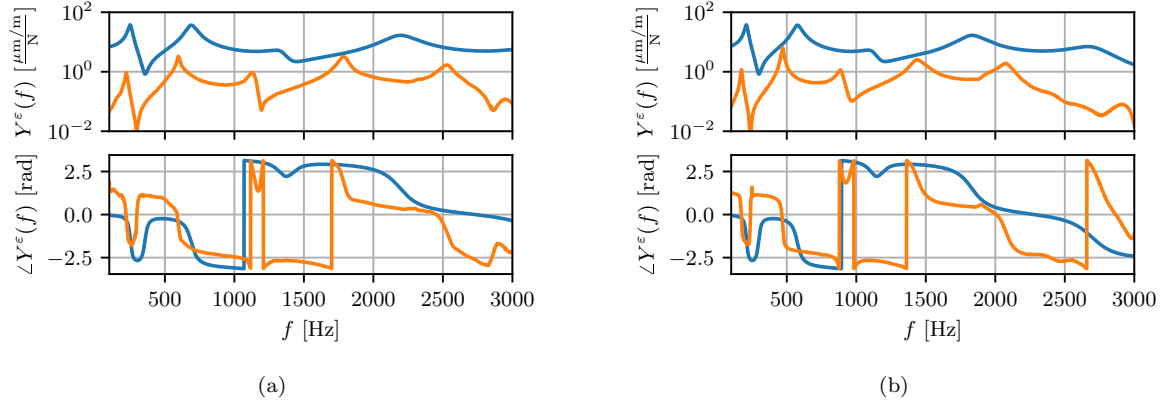


Figure 9: Comparison of experimental and numerical strain FRFs obtained with excitation at point 2 and response at point 5; a) 20 % infill, b) 40 % infill.

— - numerical model, — - experimental model

Table 3: Natural frequencies of numerical and experimental models for beams with different infill percentages.

		Mode number				
		1.	2.	3.	4.	5.
Infill 20 %	Num. [Hz]	252	690	1342	2195	3656
	Exp. [Hz]	222	592	1135	1784	2532
Infill 40 %	Num. [Hz]	210	576	1121	1832	2701
	Exp. [Hz]	174	469	889	1435	2072

pyFBS [42], and the extensions were performed using this formulation. To access the quality of the expansion process, the numerical model consists of all the DoFs obtained in the reference experiment (Fig. 10a). Here, it should be emphasized that the numerical model can include all the points in the FEM model.

To use the SEMM expansion process, the numerical model is reformulated by separating the internal and boundary DoFs to form a parent model (Fig. 10b). The parent model is a mixture of the displacement and strain FRFs. Similarly, the overlay model is formulated from the experimental model, which includes only the boundary DoFs (Fig. 10c). Three excitation points and four response points (three strain points and one displacement) comprise the overlay model. These DoFs were also present in the parent model (boundary-boundary (bb) region in Fig. 10b).

The result of the SEMM expansion process is a hybrid model, defined in all DoFs of the parent model. The accuracy of the results was assessed using the coherence criterion [12], comparing the expanded results with the reference experimental model. Values close to one indicate better agreement between the compared models, whereas values closer to zero indicate the opposite. The Table 4 quantitatively illustrates the efficiency and superiority of the SEMM expansion procedure. Despite the poor agreement between the experimental reference model and the numerical model at all DoFs, the SEMM method can be used to qualitatively expand the marginal DoFs. Only 12 measured FRFs successfully updated the remaining 44 FRFs in the numerical model. The average coherence value was increased from about 0.5 to 0.8.

Fig. 11 shows the quality of the expansion process in detail. After the expansion the FRFs on the boundary DoFs still have a very good alignment with the reference experimental model (the

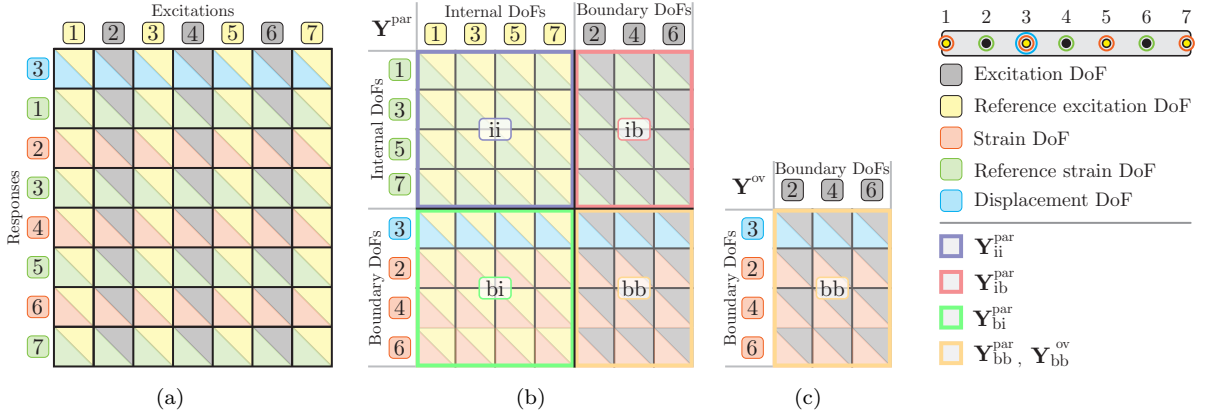


Figure 10: Admittance FRF matrices of the analyzed component; a) numerical, b) parent, c) overlay model.

Table 4: Comparison of coherence values between experimental, numerical and SEMM expanded model for beams with 20 % and 40 % infill.

infill	exp. vs num.			exp. vs SEMM		
		i	b		i	b
20 %	i	0.50	0.50	i	0.77	0.81
	b	0.52	0.53	b	0.81	1.00
40 %	i	0.50	0.50	i	0.72	0.77
	b	0.51	0.52	b	0.77	1.00

coherence value is very close to one). In the internal-boundary (ib) and boundary-internal (bi) area (Fig 10), the expansion is successful, with an average coherence of around 0.8. A poorer expansion result can be observed in the internal-internal (ii) area, where the average coherence is around 0.75 in both cases.

Based on Fig. 11 we can conclude that the expansion of the DoFs, where neither response nor excitation was acquired, is not very accurate. Moreover, a less accurate expansion can also be observed at the edge DoFs (points 1 and 7). The reason for that may be in the divergent geometry on both edges of the beam (rounded edges, final wall, etc.). All these details make the beam locally stiffer and therefore challenging to expand the dynamic properties acquired for the internal DoFs. The second reason for a poorer expansion accuracy of the edge DoF may also be the reference experimental model itself. It is very challenging to excite a structure at the edge of the beam and also the strain-gauge placement is difficult. Therefore, the reference FRF acquired at the edge of the beam may not be accurate and must be treated with caution. To avoid this problem of inconsistent measurement at the edges of the beam due to low strain values, we can simply place the strain sensors further away from the edges or use a different measurement method. It is not recommended to use such inconsistent measurements in expansion process, because they can lead to inaccurate expansion results. In such cases, it is better to omit less consistent measurements from the experimental response model and perform the expansion process using only consistent measurements, as shown in [26].

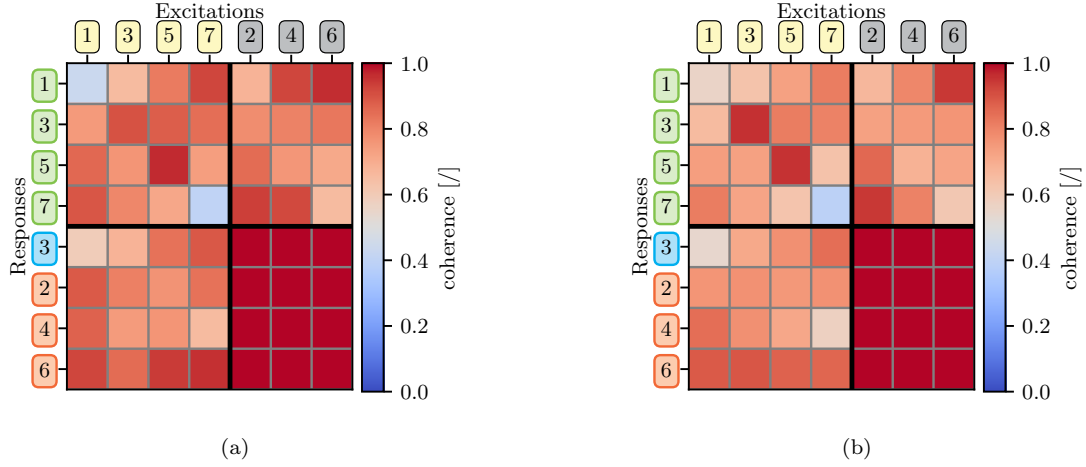


Figure 11: Average value of coherence criteria when comparing the reference experimental model with the SEMM expanded model; a) 20 % infill, b) 40 % infill.

The expansion of the displacement response (point 3 marked with blue in Fig. 11) was also successful (average coherence of expanded part is around 0.75). To achieve even better accuracy, it would be necessary to include an additional reposition point in the overlay model.

Fig. 12 shows a comparison of the SEMM expanded strain FRF and the reference experimental FRF. The expanded strain FRF belongs to the boundary-internal (bi) region of the parent model. We can see a good agreement for almost the whole observed frequency band. The discrepancy is obvious only around the third natural frequency in the region between 600 and 1500 Hz. The reason for this is that point 5 lies at the node of the third mode shape (Fig. 13) and is therefore prone to error amplification.

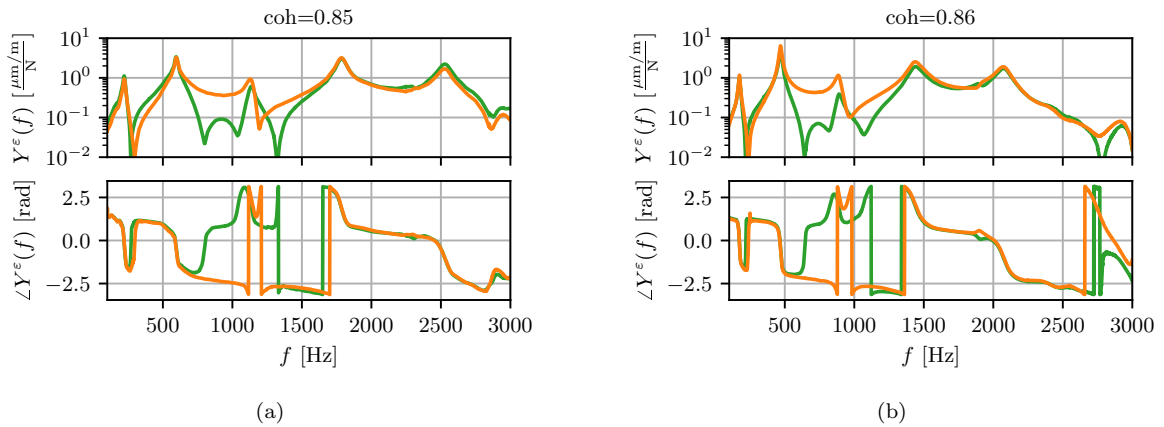


Figure 12: Comparison of SEMM expanded and reference experimental strain FRF obtained with excitation at point 2 and response at point 5; a) 20 % infill, b) 40 % infill.

— expanded model, — experimental model

Using a multi-reference modal identification method the same natural frequencies were identified on the expanded models as on the reference experimental models (Table 3). The identified strain and displacement mode shapes are simultaneously presented in Fig. 13 enabling better observability

of the dynamic properties of the analyzed structure. The displacement mode shapes are visualized with the actual displacements of the points (scaled to regions between -1 and 1). Strain mode shapes are superposed on the corresponding displacement mode shape with a color scheme, linearly interpolated between the measurement points. Strain mode shapes were also scaled to regions between -1 and 1. The PVDF strain gauges were positioned on the bottom surface of the tested beam.

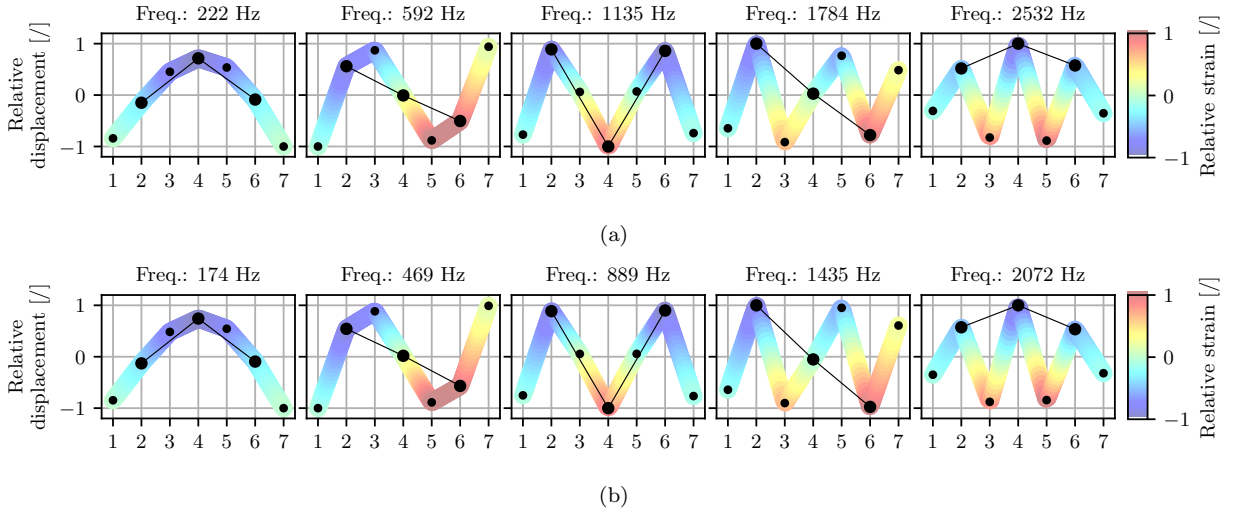


Figure 13: First five displacement and strain mode shapes of analyzed beam (strain is measured at the bottom surface of the beam); a) 20 % infill, b) 40 % infill.
 ● - location of measured strain, ● - location of expanded strain, — - aliased mode shape

Fig. 13 shows that it is possible to perfectly identify the first 5 mode shapes, even on the edge points (1 and 7), where the coherence with the experimental model was slightly less accurate. These observations are supported by the high value of the diagonal terms of the MAC criterion (around 0.99). The displacement mode shapes were identified from the FRFs obtained by the strain response on the force excitation. The same displacement mode shapes were obtained with the displacement response to the force excitation. This proves that it is possible to simultaneously expand dynamic models of different physical quantities using the proposed SEMM formulation. The conclusion could also be validated by established non-contact full-field methods, but this is beyond the scope of this article.

The black line in Fig. 13 shows the mode shape that could be identified based only on the part of the experimental model included in the overlay model. Here, we considered only three strain-response measurements from the whole experimental response model that contains 7 strain-response locations. In this case, due to the limited spatial resolution, the aliasing effect occurs; therefore, it is possible to accurately identify only the first mode shape. However, by using the SEMM expansion process it is possible to identify even higher mode shapes (Fig. 13), even though only three response points were included in the experimental (overlay) model.

6. Conclusion

This article presents an alternative approach to modeling 3D-printed structures with complex infill patterns. The strain response for a limited number of points was obtained experimentally, while the full-field response was provided using the proposed extended form of the SEMM expansion method. The proposed SEMM formulation enables the inclusion of dynamic models of complementary and also non-complementary physical quantities.

The strain response of a 3D-printed structure with a complex infill was acquired with low-cost PVDF strain sensors. Using the proposed SEMM formulation with the simplified numerical model, it was possible to accurately expand the dynamic properties of the experimental model to a denser set of DoFs. The expanded response model contained information about the strain and displacement response and the identified mode shapes match very closely with the reference experimental model.

The performed analysis indicates that the most accurate expansion is achieved at locations where measurements of either the response or the excitation were performed (at the so-called internal-boundary (ib) area and boundary-internal (bi) area). The least accurate extension quality is in the area where no measurements have been made (internal-internal (ii) area). This proves that adequate observability and controllability of the system are crucial steps for accurate expansion results.

Acknowledgements

The authors acknowledge the partial financial support from the core research funding P2-0263 and the applied research project L2-1837, both financed by ARRS, the Slovenian research agency.

References

- [1] N. Shahrubudin, T. C. Lee, R. Ramlan, An overview on 3D printing technology: Technological, materials, and applications, *Procedia Manufacturing* 35 (2019) 1286–1296.
- [2] J.-Y. Lee, J. An, C. K. Chua, Fundamentals and applications of 3D printing for novel materials, *Applied materials today* 7 (2017) 120–133.
- [3] T. Košir, J. Slavič, Single-process fused filament fabrication 3D-printed high-sensitivity dynamic piezoelectric sensor, *Additive Manufacturing* 49 (2022) 102482.
- [4] T. Barši Palmič, J. Slavič, M. Boltežar, Process parameters for FFF 3D-printed conductors for applications in sensors, *Sensors* 20 (16) (2020) 4542.
- [5] Y. Chen, D. Joffre, P. Avitabile, Underwater dynamic response at limited points expanded to full-field strain response, *Journal of Vibration and Acoustics* 140 (2018) 051016.
- [6] Y. Sun, Q. Li, Dynamic compressive behaviour of cellular materials: A review of phenomenon, mechanism and modelling, *International Journal of Impact Engineering* 112 (2018) 74–115.
- [7] M. Kucwicz, P. Baranowski, J. Małachowski, A. Popławski, P. Płatek, Modelling, and characterization of 3D printed cellular structures, *Materials & Design* 142 (2018) 177–189.
- [8] E. Provaggi, C. Capelli, B. Rahmani, G. Burriesci, D. M. Kalaskar, 3D printing assisted finite element analysis for optimising the manufacturing parameters of a lumbar fusion cage, *Materials & Design* 163 (2019) 107540.
- [9] H. Baqasah, F. He, B. A. Zai, M. Asif, K. A. Khan, V. K. Thakur, M. A. Khan, In-situ dynamic response measurement for damage quantification of 3D printed ABS cantilever beam under thermomechanical load, *Polymers* 11 (12) (2019) 2079.
- [10] B. Panda, M. Leite, B. B. Biswal, X. Niu, A. Garg, Experimental and numerical modelling of mechanical properties of 3D printed honeycomb structures, *Measurement* 116 (2018) 495–506.
- [11] G. W. Melenka, J. S. Schofield, M. R. Dawson, J. P. Carey, Evaluation of dimensional accuracy and material properties of the MakerBot 3D desktop printer, *Rapid Prototyping Journal* (2015).

- [12] M. V. van der Seijs, Experimental dynamic substructuring: Analysis and design strategies for vehicle development, Ph.D. thesis, Delft University of Technology (2016).
- [13] S. W. Klaassen, M. V. van der Seijs, D. de Klerk, System equivalent model mixing, *Mechanical Systems and Signal Processing* 105 (2018) 90–112.
- [14] J. Gietl, J. Vignola, J. Sterling, T. Ryan, Characterization of damping properties in 3D printed structures, in: *Journal of Physics: Conference Series*, Vol. 1149, IOP Publishing, 2018, p. 012002.
- [15] R. C. Parpala, D. Popescu, C. Pupaza, Infill parameters influence over the natural frequencies of ABS specimens obtained by extrusion-based 3D printing, *Rapid Prototyping Journal* (2021).
- [16] Y. Duan, B. Du, X. Shi, B. Hou, Y. Li, Quasi-static and dynamic compressive properties and deformation mechanisms of 3D printed polymeric cellular structures with kelvin cells, *International Journal of Impact Engineering* 132 (2019) 103303.
- [17] M. Vachon, Dynamic response of 3D printed beams with damping layers, Ph.D. thesis, Massachusetts Institute of Technology (2015).
- [18] R. Domingo-Roca, L. Asciak, J. Windmill, H. Mulvana, J. Jackson-Camargo, Non-destructive analysis of the mechanical properties of 3D-printed materials, *Journal of Nondestructive Evaluation* 41 (1) (2022) 1–9.
- [19] F. Medel, V. Esteban, J. Abad, On the use of laser-scanning vibrometry for mechanical performance evaluation of 3D printed specimens, *Materials & Design* 205 (2021) 109719.
- [20] C. Ao, B. Qiao, L. Chen, J. Xu, M. Liu, X. Chen, Blade dynamic strain non-intrusive measurement using L1/2-norm regularization and transmissibility, *Measurement* 190 (2022) 110677.
- [21] Y. Zhu, Y. Wang, B. Qiao, S. Fu, M. Liu, X. Lu, X. Chen, Full-field dynamic strain reconstruction of rotor blades under multi-mode vibration, *Measurement* (2022) 111670.
- [22] Y. Chen, P. Logan, P. Avitabile, J. Dodson, Non-model based expansion from limited points to an augmented set of points using Chebyshev polynomials, *Experimental Techniques* 43 (5) (2019) 521–543.
- [23] Z. Saeed, S. W. Klaassen, C. M. Firrone, T. M. Berruti, D. J. Rixen, Experimental joint identification using system equivalent model mixing in a bladed disk, *Journal of Vibration and Acoustics* 142 (5) (2020).
- [24] T. Bregar, K. Zaletelj, G. Čepon, J. Slavič, M. Boltežar, Full-field FRF estimation from noisy high-speed-camera data using a dynamic substructuring approach, *Mechanical Systems and Signal Processing* 150 (2021) 107263.
- [25] D. Ocepek, M. Kodrič, G. Čepon, M. Boltežar, On the estimation of structural admittances from acoustic measurement using a dynamic substructuring approach, *Applied Acoustics* 180 (2021) 108115.
- [26] M. Kodrič, G. Čepon, M. Boltežar, Experimental framework for identifying inconsistent measurements in frequency-based substructuring, *Mechanical Systems and Signal Processing* 154 (2021) 107562.
- [27] Z. Saeed, C. M. Firrone, T. M. Berruti, Hybrid Numerical-Experimental Model Update Based on Correlation Approach for Turbine Components, *Journal of Engineering for Gas Turbines and Power* 143 (4) (02 2021).
- [28] M. Kodrič, T. Bregar, G. Čepon, M. Boltežar, An expansion based on system equivalent model mixing: From a limited number of points to a full-field dynamic response, *Measurement* 190 (2022) 110522.
- [29] Y. Xin, H. Sun, H. Tian, C. Guo, X. Li, S. Wang, C. Wang, The use of polyvinylidene fluoride (PVDF) films as sensors for vibration measurement: A brief review, *Ferroelectrics* 502 (1) (2016) 28–42.
- [30] T. Bregar, B. Starc, G. Čepon, M. Boltežar, On the use of PVDF sensors for experimental modal analysis, in: *Topics in Modal Analysis & Testing*, Volume 8, Springer, 2021, pp. 279–281.
- [31] L. Vári, P. Heyns, Using strain modal testing, *Proceedings of the 12th International Modal Analysis* 2251 (1994) 1264.
- [32] F. Dos Santos, B. Peeters, J. Lau, W. Desmet, L. Góes, An overview of experimental strain-based modal analysis methods, in: *Proceedings of the International Conference on Noise and Vibration Engineering (ISMA)*, Leuven, Belgium, 2014, pp. 2453–2468.
- [33] T. Kranjc, J. Slavič, M. Boltežar, The mass normalization of the displacement and strain mode shapes in a strain experimental modal analysis using the mass-change strategy, *Journal of Sound and Vibration* 332 (26) (2013) 6968–6981.
- [34] D. de Klerk, D. J. Rixen, J. de Jong, The frequency based substructuring (FBS) method reformulated according to the dual domain decomposition method, in: *Proceedings of the 24th International Modal Analysis Conference, A Conference on Structural Dynamics*, 2006, pp. 1–14.
- [35] D. de Klerk, D. J. Rixen, S. Voormeeren, General framework for dynamic substructuring: history, review and classification of techniques, *AIAA journal* 46 (5) (2008) 1169–1181.
- [36] S. Klaassen, M. V. van der Seijs, Introducing SEMM: A novel method for hybrid modelling, in: *Dynamics of Coupled Structures*, Volume 4. Conference Proceedings of the Society for Experimental Mechanics Series, Springer International Publishing, 2018, pp. 117–125.
- [37] A. Elliott, A. Moorhouse, G. Pavić, Moment excitation and the measurement of moment mobilities, *Journal of*

- sound and vibration 331 (11) (2012) 2499–2519.
- [38] F. L. M. d. Santos, B. Peeters, M. Menchicchi, J. Lau, L. Gielen, W. Desmet, L. C. S. Góes, Strain-based dynamic measurements and modal testing, in: *Topics in Modal Analysis II*, Volume 8, Springer, 2014, pp. 233–242.
 - [39] M. Specialties, Piezo film sensors technical manual, *Measurement* 57 (2006).
 - [40] F. L. dos Santos, B. Peeters, J. Debille, C. Salzano, L. Carlos, S. Góes, W. Desmet, The use of dynamic strain sensors and measurements on the ground vibration testing of an f-16 aircraft, in: *Proceedings of the 16th International Forum on Aeroelasticity and Structural Dynamics*, 2015.
 - [41] K.-C. Chuang, C.-C. Ma, H.-C. Liou, Experimental investigation of the cross-sensitivity and size effects of polyvinylidene fluoride film sensors on modal testing, *Sensors* 12 (12) (2012) 16641–16659.
 - [42] T. Bregar, A. El Mahmoudi, M. Kodrič, D. Ocepek, F. Trainotti, M. Pogačar, M. Göldeli, G. Čepon, M. Boltežar, D. J. Rixen, pyFBS: A python package for frequency based substructuring, *Journal of Open Source Software* 7 (69) (2022) 3399.